Integer and fractional quantum hall effects in lattice magnets

Venderbos, J.W.F.

Part II

Lattice Fractional Quantum Hall Effects

CHAPTER 5

TOPOLOGICAL BANDS AND ORBITAL DEGREES OF FREEDOM

5.1 Introduction

Investigating the repercussions of topology on the electronic states in condensed matter systems has a long and rich history. The Integer Quantum Hall (IQH) effect, discovered [75] in 1980, was soon understood to be a profound manifestation of the topological properties of the Landau levels. The quantized Hall conductance was shown to be a topological invariant that classifies the ground state [16]. Later that decade, Haldane [76] showed that the IQH state is not restricted to two-dimensional (2D) electron gases in a strong magnetic field. It can also be realized in lattice systems without Landau levels, by introducing electrons on a lattice with complex hoppings that break time-reversal symmetry. In recent years, topologically nontrivial electronic phases were moreover discovered in time-reversal invariant insulators [1, 3, 4, 72], leading to the Quantum Spin Hall effect in 2D [6, 7] and to the existence of protected 2D Dirac fermions on the surface of 3D topological insulators [12, 111] and a related quantum Hall effect [112].

These presently much studied 2D and 3D topological insulators are time-reversal invariant lattice systems that can therefore be perceived as a further generalization of the Quantum Hall states. The generalization of Fractional Quantum Hall (FQH)

states, the fractional counterpart of the IQH states, was considered only very recently [87, 108, 113]. Such a lattice FQH effect will be quite different from the ordinary FQH in 2D electron gases, for instance requiring a variational wavefunction distinct from the Laughlin wave function [114–116], and it can occur without magnetic field and potentially at high temperature [87, 108, 113]. Its realization in a material system would offer an exciting prospect for quantum computation, since the presence of non-Abelian FQH states allows for the creation of topologically protected qbits [117]. Creating the analogue of the FQH effect in a lattice system requires the fractional filling of topologically nontrivial bands, which should be very narrow [87, 108, 113], so that the electron-electron interactions can dominate over the kinetic energy and induce FQH states [104].

The theoretical approach used to progress toward this goal so far relies on the fine-tuning of the electron kinetic energy in model Hamiltonians containing bands with the correct topological properties [87, 108, 113]. Such a flattening procedure of the bands usually requires tuning (very) long-range hopping parameters to a set of quite peculiar strengths, which in real materials represents a rather formidable challenge from an experimental point of view.

We consider orbital degrees of freedom as an alternative agent for band flattening. Orbitals naturally occur in many transition metal (TM) compounds, which at the same time feature strong electron-electron interactions [118]. We concentrate on manganites, where Mn^{3+} ions are in a high-spin $3d^4$ configuration, with three electrons in the more localized t_{2g} states forming a spin of 3/2 and one electron in either of the two more itinerant e_g orbitals ferromagnetically coupled to this spin. Apart from other $3d$ systems besides Mn, the versatile class of TM oxides also contains $4d$ and $5d$ materials with orbital degrees of freedom, of which ruthenates [119] and iridates [120, 121] are important examples.

We will show that in the presence of a chiral spin texture, such an orbital make-up leads to nearly flat topologically nontrivial bands. It is well established that geometric frustration may stabilize non-coplanar spin-chiral magnetic textures when itinerant electrons couple to localized spins [29–33]. The Berry phase acquired by the electrons then leads to topologically nontrivial bands [30, 31, 78, 85, 97]. The pronounced spatial anisotropy of the e_g and t_{2g} orbitals strongly affects the symmetry of hopping integrals, even suppressing hopping completely along some directions.This can result in very flat bands like the dispersionless bands found in several multi-orbital TM compounds – a number of antiferromagnetic phases in cubic manganites are stabilized by such a mechanism [122, 123]. Here, we report a strong orbital-induced flattening of topological bands in spin-chiral phases on frustrated kagome and triangular lattices, demonstrating that orbital degrees of freedom of transition-metal ions generically provide a route to realizing a lattice version of the FQH effect. We also present indications that residual interactions can then induce a FQH state.

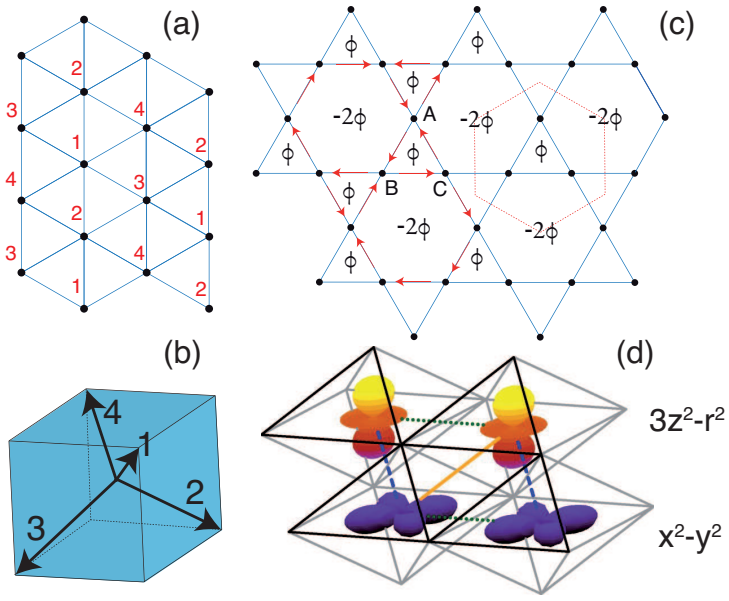

Figure 5.1: (a) Chiral spin ordering on the triangular lattice. (b) Spins forming a regular tetrahedron, numbers refer to sites in (a). (c) Flux-phase state on the kagome lattice. The unit cell is indicated by the dashed hexagon and the gauge choice by arrows; a flux ϕ threads each triangle. (d) Nearest-neighbor hopping geometry in lattices with triangular symmetry. Grey lines illustrate the oxygen octahedra, black front facets illustrate the triangular geometry. Thick dotted, dashed and solid lines indicate the bonds corresponding to the hopping matrices $\hat{T}_1$, $\hat{T}_2$, and $\hat{T}_3$. Two $d_{3z^2-r^2}$ (top) and $d_{x^2-y^2}$ (bottom) orbitals are also shown.

5.2 Chiral spin ordering

We first summarize the situation on the triangular and kagome lattices for mobile charge carriers without orbital degrees of freedom in presence of a nontrivial spin-texture. The Kondo Lattice Model, which describes the interaction between localized (t_{2g}) spins and itinerant (e_g) electrons, exhibits a topologically nontrivial chiral spin state on the triangular lattice [30–32]. This state has a four–sub-lattice ordering, illustrated in Fig. 5.1(a) and a finite scalar spin chirality $\langle \vec{S}_1 \cdot \vec{S}_2 \times \vec{S}_3 \rangle \neq 0$ for spins on the corners of triangles. The situation then becomes equivalent to electrons hopping on a triangular lattice with a fictitious gauge flux of $\phi = \pi/2$ threading each triangle, see Fig. 5.1. The effective electronic Hamiltonian has a two-site unit cell [30] and two bands, with Chern numbers ± 1, are separated by a gap. On the kagome lattice, a staggered flux pattern, shown in Fig. 5.1, can result from topologically nontrivial spin states, where a flux ϕ threads each triangle and a flux -2ϕ each hexagon [85]. Time-reversal symmetry is broken for $\phi \neq 0, \pi$ and two gaps open, leading to three bands. The middle band has zero Chern number, but the lowest and highest are topologically nontrivial with $C = \mp \mathrm{sgn}(\sin\phi)$ [85]. However, all topologically nontrivial bands have a considerable dispersion on both lattices, which we will now show to be substantially reduced by the presence of an orbital degree of freedom.

5.3 Orbital degrees of freedom

In many TM oxides, the TM ions are inside oxygen octahedra, which are edge-sharing in a triangular lattice, see Fig. 5.1. The cubic symmetry splits the TM d levels into three t_{2g} and two e_g orbitals. We focus mainly on the latter, but later also demonstrate an analogous effect for the former. Collecting the e_g orbital degree of freedom in a pseudo-spin $\tau^z = \pm 1$ object we write

$$|e_g\rangle = \begin{bmatrix} |3z^2 - r^2\rangle \\ |x^2 - y^2\rangle \end{bmatrix} \equiv \begin{bmatrix} |z\rangle \\ |x\rangle \end{bmatrix}. \tag{5.1}$$

Along the $\vec{a}_1 = (0, 1)$ direction, indicated by a dotted line in Fig. 5.1, hopping for e_g orbitals conserves orbital flavor and is given by t (t') for the $|x^2 - y^2\rangle$ ($|3z^2 - r^2\rangle$) orbital. This is captured by the hopping matrix acting on the orbital pseudospin

$$\hat{T}_1 = \begin{bmatrix} t' & 0 \\ 0 & t \end{bmatrix}. \tag{5.2}$$

Hoppings along the other two bonds are obtained by a rotation in orbital space, which are representations of real space rotations in pseudospin space. As the pseudospin

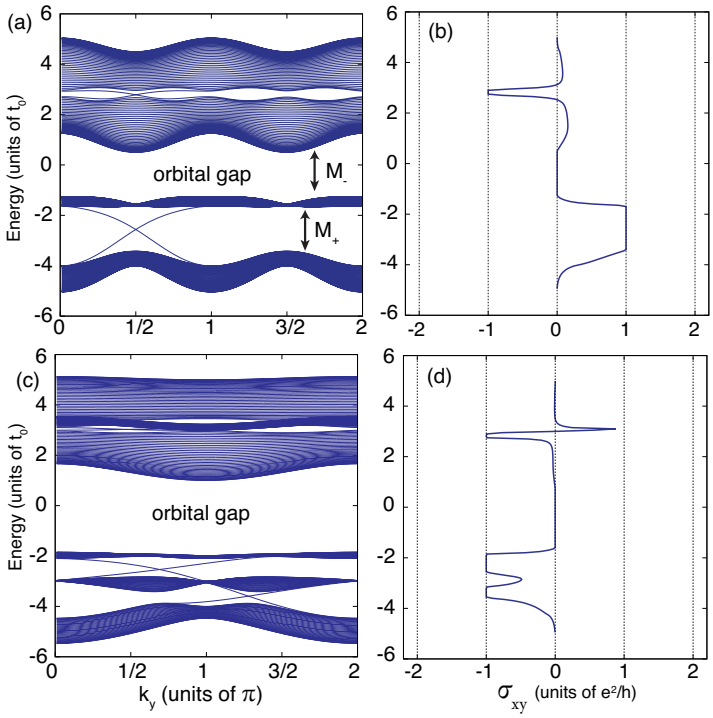

Figure 5.2: Top: kagome lattice, bottom: triangular lattice. Left: bands of a strip geometry, clearly showing the chiral edge states of the flattened bands. Right: off-diagonal Hall conductivity as function of chemical potential, providing the Chern numbers for the flat bands. For the Kagome lattice $t' = -0.46$, $\Delta = 2.75$, $\phi = \pi/4$ and for the triangular case $t' = -0.46$, $\Delta = 2.5$.

must transform as a real representation rotations over an angle θ are implemented by the matrix $e^{-i\theta\tau^y}$. Using this one may obtain for the other directions $\vec{a}_2$ and $\vec{a}_3$

$$\hat{T}_2 = \frac{1}{4}\begin{pmatrix} t'+3t & \sqrt{3}(t'-t) \\ \sqrt{3}(t'-t) & 3t'+t \end{pmatrix},$$
$$\hat{T}_3 = \frac{1}{4}\begin{pmatrix} t'+3t & -\sqrt{3}(t'-t) \\ -\sqrt{3}(t'-t) & 3t'+t \end{pmatrix}, \tag{5.3}$$

We use t as unit of energy and vary the material-dependent ratio t'/t between -1 and 1, concentrating on $t'/t < 0$ inferred from direct overlaps of the orbitals. For our fillings of approximately one electron per site, the Jahn-Teller effect is important and can induce a uniform crystal field

$$\hat{H}_{\rm JT} = \Delta(\hat{n}_x - \hat{n}_z) \tag{5.4}$$

lifting orbital degeneracy.

Even though the spin pattern underlying the chiral spin state on the triangular lattice has a four-site unit cell, the electronic Hamiltonian has only a two-site unit cell and can thus be described by a 2×2 matrix if the original model is a one-band model. [30] With an underlying multi-orbital Hamiltonian, this becomes a Hamiltonian matrix consisting of four blocks ($\mathcal{H}_{11}(\vec{k})$, $\mathcal{H}_{12}(\vec{k})$, $\mathcal{H}_{21}(\vec{k})$ and $\mathcal{H}_{22}(\vec{k})$), where the blocks refer to the lattice sites of the spatial unit cell and are matrices in orbital space, leading to

$$\mathcal{H}(\vec{k}) = \begin{bmatrix} \mathcal{H}_{\rm JT} + \mathcal{H}_{11}(\vec{k}) & \mathcal{H}_{12}(\vec{k}) \\ \mathcal{H}_{21}(\vec{k}) & \mathcal{H}_{\rm JT} + \mathcal{H}_{22}(\vec{k}) \end{bmatrix} \tag{5.5}$$

where the blocks are given by

$$\mathcal{H}_{11} = -\mathcal{H}_{22} = -2\hat{T}_1 \cos(\vec{k}\cdot\vec{a}_3), \tag{5.6}$$
$$\mathcal{H}_{12} = \mathcal{H}_{21}^\dagger = -2\hat{T}_2 \cos(\vec{k}\cdot\vec{a}_1) - 2i\hat{T}_3 \cos(\vec{k}\cdot\vec{a}_2)$$

The hopping matrices T_i are the 2×2 matrices Eq. (5.3) for e_g electrons defined above. The matrices $H_{\rm JT}$ given by the crystal field refer to Eqs. (5.4). Figure 5.2 shows the energy bands calculated for a strip geometry, with periodic boundary conditions in one direction and two edges in the orthogonal direction. For a large enough crystal-field splitting $\Delta > t, t'$, a gap separates bands with different orbital character. Within each subsystem, chiral magnetic order induces a further splitting into two topologically nontrivial bands with Chern numbers $C = \pm 1$. This is unambiguously indicated by the topological edge states connecting the bands with $C > 0$ and

$C < 0$ in Fig. 5.2(a). The transverse Hall conductivity σ^n_{xy} is shown in Fig. 5.2(b) and directly reflects the topological character of the bands. The Hall conductivity is calculated as

$$\sigma^n_{xy} = -i \sum_{\vec{k}, m \neq n} \frac{\langle m\vec{k}|J_x|n\vec{k}\rangle\langle n\vec{k}|J_y|m\vec{k}\rangle - \text{h.c.}}{(E_n(\vec{k}) - E_m(\vec{k}))^2} f(E_n(\vec{k})) \tag{5.7}$$

where $|n\vec{k}\rangle$ are the eigenstates of the Hamiltonian (n being the band index) and $E_n(\vec{k})$ are the corresponding eigenvalues. The current operators J_i are obtained from

$$\hat{J}_i = \sum_{\vec{k}} \hat{\psi}^\dagger(\vec{k}) \frac{\partial \mathcal{H}(\vec{k})}{\partial k_i} \hat{\psi}(\vec{k}). \tag{5.8}$$

The topological character of the bands is related to the Hall conductivity by the identity

$$\begin{aligned} \sigma^n_{xy} &= \frac{e^2}{h} C_n = \frac{-ie^2}{2\pi h} \int_{BZ} d^2k \ \text{Tr}\left[\mathcal{F}_{xy}\right] \\ &= \frac{-ie^2}{2\pi h} \int_{BZ} d^2k \sum_{n \in \text{occ}} \partial_x \mathcal{A}^{nn}_y - \partial_y \mathcal{A}^{nn}_x \end{aligned} \tag{5.9}$$

where C_n is the Chern number of the n-th band. The non-Abelian Berry connection $\mathcal{A}^{mn}_i$ is defined as

$$\mathcal{A}^{mn}_i = -i\langle m\vec{k}|\partial_i|n\vec{k}\rangle, \tag{5.10}$$

from which the field strength $\mathcal{F}^{mn}_{ij}$ is derived as

$$\mathcal{F}_{ij} = \partial_i \mathcal{A}_j - \partial_j \mathcal{A}_i + i[\mathcal{A}_i, \mathcal{A}_j]. \tag{5.11}$$

The gap between the topological bands is smaller in the upper ($x^2 - y^2$) sector, but robust between the two $3z^2 - r^2$ bands below the crystal-field gap. The upper band of the $3z^2 - r^2$ sector with $C = -1$, has a weak dispersion, becoming nearly flat for $t' \approx -t/2$, see Fig. 5.2(a). The figure of merit quantifying the flatness is the ratio of the gaps M separating it from other bands to its band width W. Here we monitor both the 'topological' gap (M_+), which is induced by chiral order and the 'trivial' crystal-field gap (M_{-1}), which separates it from the $x^2 - y^2$ sector above. Figure 5.3(a) shows these ratios depending on t' and Δ, the relevant figure of merit is the smaller of the two ratios M_+/W and M_{-1}/W. It is appreciable in a broad range of Δ and t', reaching a maximum of ~ 4.25 for $\Delta = 2.5$ and $t' = -0.45$.

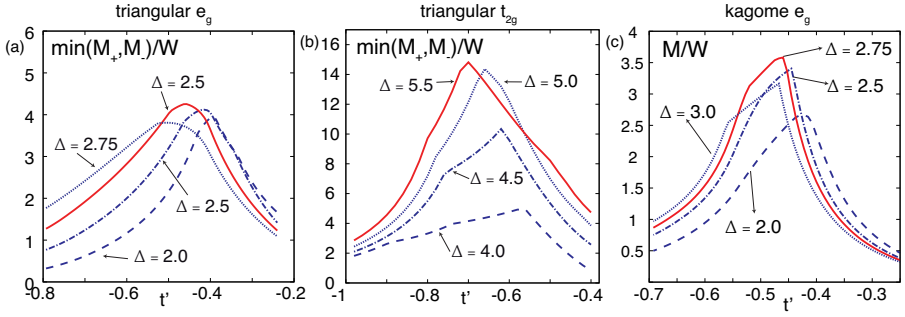

Figure 5.3: (a) The smallest band gap over bandwidth ratios for e_g electrons the triangular lattice, for the gaps M_+ and M_- indicated in Fig. 5.2(a). (b) The same for t_{2g} electrons on a triangular lattice and (c) for e_g on the kagome lattice. Orbital splittings are indicated by Δ.

In addition to e_g orbitals we may also consider t_{2g} orbitals. Collecting them in a vector again we write

$$|t_{2g}\rangle = \begin{bmatrix} |xy\rangle \\ |xz\rangle \\ |yz\rangle \end{bmatrix} \equiv \begin{bmatrix} |a\rangle \\ |b\rangle \\ |c\rangle \end{bmatrix} . \tag{5.12}$$

The t_{2g}-hopping matrices are given by the expressions

$$\hat{T}_1 = \begin{pmatrix} t' & 0 & 0 \\ 0 & 0 & t \\ 0 & t & 0 \end{pmatrix}, \quad \hat{T}_2 = \begin{pmatrix} 0 & 0 & t \\ 0 & t' & 0 \\ t & 0 & 0 \end{pmatrix}, \quad \hat{T}_3 = \begin{pmatrix} 0 & t & 0 \\ t & 0 & 0 \\ 0 & 0 & t' \end{pmatrix}, \tag{5.13}$$

and consist of inter-orbital hopping t (primarily via ligand oxygen ions [124]) and orbital-conserving hopping t' due to direct overlap [125]. In a three-fold symmetry, the t_{2g} manifold is further split into one a_{1g} and two e'_g states separated by a crystal field $\hat{H}_{\rm JT}$. The crystal field related to elongating or shortening the octahedra is naturally expressed in the $\{a_{1g}, e'_{g+}, e'_{g-}\}$ basis reflecting the triangular symmetry. It is then explicitly given by $\hat{H}_{\rm JT} = \Delta(\hat{n}_{e_{g+}} + \hat{n}_{e_{g-}} - 2\hat{n}_{a_{1g}})/3$, which can be expressed in the original $\{xy, xz, yz\}$ basis via the basis transformation defined in Ref. [125] and becomes

$$\mathcal{H}_{\rm JT} = -\frac{\Delta}{3} \begin{pmatrix} 0 & 1 & 1 \\ 1 & 0 & 1 \\ 1 & 1 & 0 \end{pmatrix} \tag{5.14}$$

Qualitatively, we find similar behavior as for e_g orbitals, but the figure of merit reaches $M/W \approx 14$, see Fig. 5.3(b). This extraordinarily large M/W reflects the very large spatial anisotropy of t_{2g} hopping integrals, well-known in triangular vanadates [124] and cobaltates [125].

After discussing the triangular lattice, we now come to e_g orbitals on the kagome lattice illustrated in Fig. 5.1(b). The lattice has a three-site unit cell, and one proceeds with an approach analogous to the two-site unit cell discussed above. The sublattices of the kagome lattice are labeled as A, B and C, and taking the orbital degree of freedom into account the fermion operator becomes

$$\hat{\psi}^\dagger(\vec{k}) = (\hat{\psi}^\dagger_{Az}(\vec{k}), \hat{\psi}^\dagger_{Ax}(\vec{k}), \hat{\psi}^\dagger_{Bz}(\vec{k}), \hat{\psi}^\dagger_{Bx}(\vec{k}), \hat{\psi}^\dagger_{Cz}(\vec{k}), \hat{\psi}^\dagger_{Cx}(\vec{k}))$$

and the Hamiltonian is given by

$$\mathcal{H}(\vec{k}) = \begin{bmatrix} \mathcal{M}_0 & \mathcal{M}_1 & \mathcal{M}_3^\dagger \\ \mathcal{M}_1^\dagger & \mathcal{M}_0 & \mathcal{M}_2 \\ \mathcal{M}_3 & \mathcal{M}_2^\dagger & \mathcal{M}_0 \end{bmatrix} \tag{5.15}$$

where the orbital matrices $\mathcal{M}$ take the form

$$\begin{aligned} \mathcal{M}_0 &= \mathcal{H}_{\text{JT}} \\ \mathcal{M}_i(\vec{k}) &= 2\hat{T}_i \cos(\vec{k}\cdot\vec{a}_i) e^{-i\phi/3}. \end{aligned} \tag{5.16}$$

Bands are again separated by the crystal field into two parts with a different orbital character, see Fig. 5.2. While the x^2-y^2 sector is hardly gapped, the $3z^2-r^3$ sector shows three sub-bands with $C = 0, \pm 1$ similar to the one-band model [85]. Again, the topological character can be inferred from edge states and is confirmed by the Hall conductivity shown in Fig. 5.2(d) and as for the triangular lattice, the top band of the $3z^2 - r^3$ sector (with $C = +1$) is very flat for $t' \approx -t/2$. The figure of merit M/W is plotted in Fig. 5.3(c); it reaches values up to ~ 3.5 for $\Delta = 2.75$ and $t' = -0.45$, compared to $W/M \lesssim 1$ in the one-band model without orbital degrees of freedom.

5.4 FQH state induced by residual interactions

After showing that orbital degrees of freedom can lead to flat bands with Chern number $C \neq 0$, we analyze the impact of Coulomb repulsion on the triangular-lattice e_g system. We include electron-electron interactions

$$\hat{H}_{\text{int}} = U \sum_i \hat{n}_{ix}\hat{n}_{iz} + V \sum_{\langle i,j\rangle,\alpha\beta} \hat{n}_{i\alpha}\hat{n}_{j\beta} \ , \tag{5.17}$$

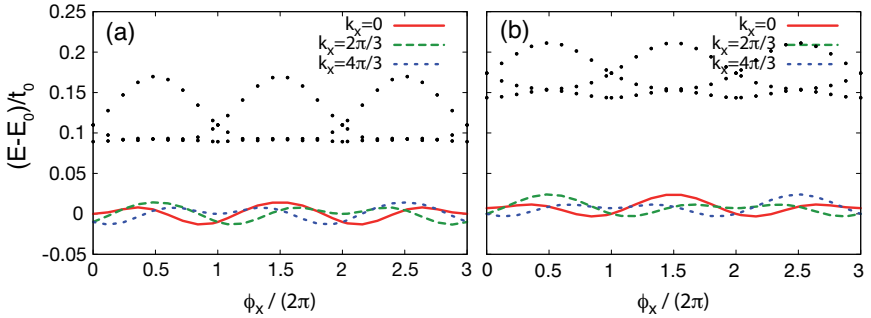

Figure 5.4: Lowest energies of the interacting e_g system on the triangular lattice, depending on flux inserted for (a) $U = 2$, $V = 1$, and (b) $U = 4$, $V = 2$. The ED results presented here were obtained for a 2×6 system with $t'/t = -0.46$ and $\Delta = 1.5$.

where $\hat{n}_{i\alpha}$ is the electron density in orbital α on site i, U acts on electrons occupying two orbitals on the same site, and V gives the nearest-neighbor (NN) interaction. It should be noted that the nearest-neighbor interaction V is defined on the original underlying triangular lattice, i.e., the same interaction V acts both between the two real-space sites of the same unit cell and between sites in different unit cells, if these sites are nearest-neighbors on the triangular lattice. Following Refs. [104, 108], we use Exact Diagonalization (ED) to study signatures of FQH-like states for a filling $1/3$ of the topologically nontrivial flat band. When adding these interactions to the Hamiltonian, we have to take into account that U implies an additional energy cost for electrons in the energetically higher $x^2 - y^2$ orbitals, thus changing the crystal field splitting Δ. In our ED calculations, we therefore reduce Δ from the value $\Delta = 2.5$ that would give the flattest band.

Exact diagonalization studies were only performed for the e_g triangular lattice model, because this case has the smallest unit cell of the models considered here. Even so, only very small systems are accessible. We use $N_x \times N_y$ real-space sites, giving $N_c = N_s/2 = N_x \times N_y/2$ unit cells of the chiral phase, but $N_{sp} = 2N_s$ "generalized" orbitals determining the size of the Hilbert space. There is no spin degree of freedom, i.e., we study spinless fermions. The filling is the one expected to correspond to the simplest FQH state, i.e., $\nu = 1/3$ filling of the nearly flat band. Since this band is close to half filling, this also implies a total filling of $1/3$, i.e., an electron number of $N_e = N_{sp}/3$.

Due to the large number of "generalized" orbitals per unit cell and due to the fact that our total electron filling is closer to half filling (which additionally increases

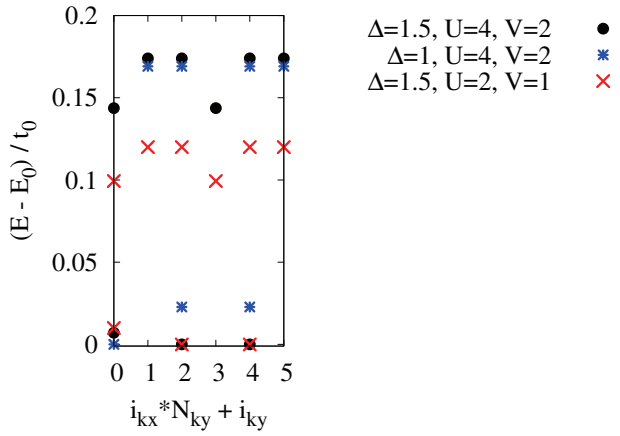

Figure 5.5: Lowest energies of the interacting e_g system on the triangular lattice for the various total momenta of the 6×2 lattice for a few parameter sets, $t'/t = -0.46$

the size of the Hilbert space), the lattice sizes accessible are considerably smaller than for models considered previously. [104, 108] Since we need the total number of sites to be divisible by 3 in order to obtain $1/3$ filling and since we also want bot N_x and N_y to be even, we consider a 2×6 "ladder" ($N_c = 6$, $N_{sp} = 24$). For simplicity, we "distort" the triangular lattice and assume the x direction to lie along $\vec{a}_1$ and the y direction along $\vec{a}_2$ to be orthogonal, the third nearest-neighbor bond is still determined by $\vec{a}_3 = \vec{a}_1 - \vec{a}_2$.

The Hamiltonian is invariant under translations, hence total momentum constitutes a good quantum number. Figure 5.5 shows the lowest two eigenvalues within the sectors corresponding to the total momenta possible on a 6×1 chain (the two sites in y-direction define the two-site unit cell in real space), and one clearly sees three low-energy states separated from the remaining spectrum by a gap. We find an approximate threefold ground-state manifold, which is an indication for the topological degeneracy of a FQH state. The three "ground states" cross each other upon inserting a magnetic flux [126], see Fig. 5.4. Adiabatic flux insertion is implemented by dividing the total flux ϕ in smaller phases ϕ/N_x added to each hopping process, which is equivalent to using twisted boundary conditions and preserves translational invariance. This replaces the two hopping matrices whose corresponding lattice vectors have a component along $\vec{a}_1$, i.e., T_1 and T_3 by $T_1 \mathrm{e}^{i\phi/N_x}$ and $T_3 \mathrm{e}^{i\phi/N_x}$. Figure 4 in the main text shows the evolution of the ground state manifold as function of

the inserted flux. The system assumes an equivalent, yet not identical, state after one unit $\phi = 2\pi$ of flux is threaded through the system, meaning that states in the ground state manifold have switched places. After 3 periods of flux insertion, where 3 corresponds to the inverse of the filling fraction, ν^{-1}, with $\nu = 1/3$, we recover an identical situation as zero flux. This is in agreement with results for other models [105, 108]. Figure 5.6 shows the same for various other parameter sets, indicating that the behavior is stable. This level crossing of the degenerate many body ground state manifold reveals the existence of the FQH ground state, provided that the spectral gap persists in the thermodynamic limit, in order to unambiguously exclude a charge density wave [105].

5.5 Discussion

The flattening due to the orbital degrees of freedom presented here can be further enhanced by introducing and fine-tuning longer-range hopping integrals, as in one-band models. Perfectly flat and topologically nontrivial bands ($M/W \to \infty$) can in principle be obtained by allowing for arbitrarily long-range hoppings [87]. We do not explore this here, as we aim to show that the anisotropy inherent in d-orbital degrees of freedom can robustly flatten topological bands even with purely NN hopping, and obtain flattening ratios up to $M/W \approx 4$ ($M/W \approx 14$) for e_g (t_{2g}) systems.

Orbital degrees of freedom are directly relevant to numerous well-known TM systems. Manganese compounds alone, which closely correspond to the e_g model studied here, occur in a variety of crystal structures: in simple cubic or square lattices in $La_{1-x}Sr_xMnO_3$ and $LaSrMnO_4$, honeycomb in e.g. Li_2MnO_3 or $(Bi_3Mn_4O_{12})NO_3$ but also in strongly frustrated pyrochlore lattices as in e.g. $Ti_2Mn_2O_7$ and in triangular lattices as in $YMnO_3$. The pyrochlore lattice, in particular, is realized by the B-site TM ions in the very common spinel crystal structure, and can be thought of as consisting of kagome and triangular layers stacked along the $(1, 1, 1)$ direction. Singling out the triangular or kagome layers, possibly via chemical substitution or controlled monolayer growth, may thus lead to systems similar to the ones studied here.

A FQH ground state needs an interaction V that exceeds the bandwidth ($V > W$), but remains smaller than the gap ($V < M$) so that bands are not mixed. Fortunately, TM oxides have substantial Coulomb interactions and NN repulsion V can become as large as or larger than the hoppings. On the other hand, is is almost always smaller than onsite repulsion, which increases one of the two gaps delimiting the flat band.The remaining challenge is thus to keep the effective interaction small compared to the gap separating the bands with $C = \pm 1$. A large figure of merit M/W provides a large window for this separation of energy scales $W < V < M$ and our ED results

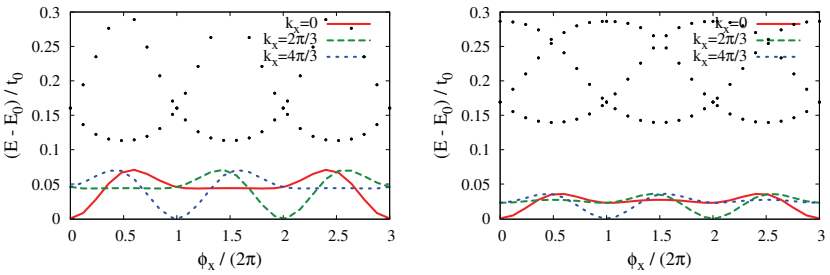

(a) $\Delta = 0.5, U = 4, V = 2$ (b) $\Delta = 1, U = 4, V = 2$

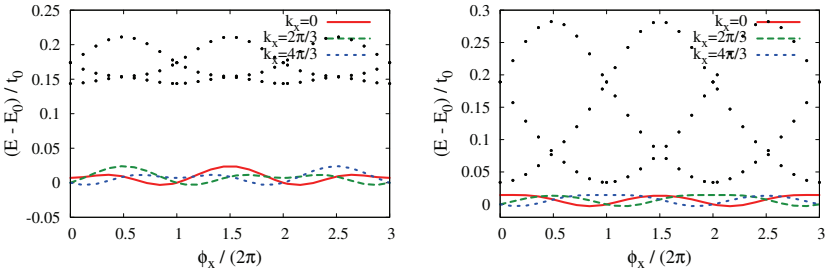

(c) $\Delta = 1.5, U = 4, V = 2$ (d) $\Delta = 2, U = 4, V = 2$

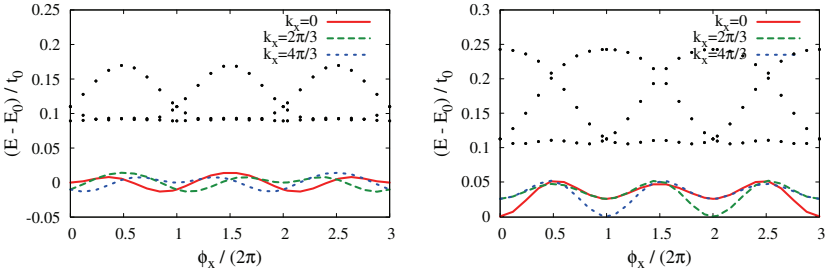

(e) $\Delta = 1.5, U = 2, V = 1$ (f) $\Delta = 1, U = 2, V = 1$

Figure 5.6: Lowest energies of the interacting e_g system on the triangular lattice, depending on flux inserted for various parameter sets. (c) and (e) are given in the main text as Fig. 4(a,b). The ED results presented here were obtained for a 2×6 system with $t'/t = -0.46$.

in Fig. 5.4 suggest that one indeed has some flexibility in this regard, as interactions differing by a factor of two lead to similar results. The crystal field splitting needed to obtain the desired flattening can be varied by applying (chemical) pressure. Finally, many of these materials, manganites in particular, are easy to dope which allows control of the (fractional) band filling.

Theoretically, there is no fundamental objection to the realization of lattice FQH states, but it remains an intriguing challenge from an experimental and practical point of view. We have demonstrated here that d-orbital degrees of freedom, ubiquitous in TM compounds, substantially narrow the topologically nontrivial bands of electrons moving in a background of non-coplanar spins. The separation of energy scales is comparable to that achievable by long-range hopping, and we find signatures of a FQH-like ground state. In the search for the lattice FQH effect, geometrically frustrated TM compounds with an orbital degree of freedom thus come to the fore as a promising class of candidate systems.